fractal and fractional

Article

Fractal Study of the Development Law of Mining Cracks

Jinsui Wu [1,2], Dongyu Xie [1], Sihai Yi [1,*], Shangxian Yin [1,2], Dezhi Hu [1], Yuanyuan Li [1] and Yun Wang [1]

[1] School of Safety Engineering, North China Institute of Science and Technology, Langfang 065201, China; jinsui_wu@126.com (J.W.); dongyux23@163.com (D.X.); yinshx03@126.com (S.Y.); hudezhi@ncist.edu.cn (D.H.); liyy@ncist.edu.cn (Y.L.); pw_y_c@163.com (Y.W.)
[2] Hebei State Key Laboratory of Mine Disaster Prevention, Langfang 065201, China
* Correspondence: tsyisihai@163.com

Abstract: Studying mining fracture development is vital for geotechnical and mining engineering and geological disaster prevention. This research assesses crack effects on rock mass stress equilibrium during coal mining, potentially causing geological disasters such as land subsidence and landslides. Using fractal geometry theory, the present study investigates the development of horizontal and vertical mining cracks, revealing their propagation patterns. The fractal dimension generally increases as the propulsion distance increases; however, fluctuations vary from 250 to 287.5 m, forming a wavering line chart. The proportion of mining fracture area relative to mining space area increases with greater propulsion distance, indicating expanded upward mining space due to separation layers. The horizontal distribution of mining cracks persists, while the vertical distribution decreases, suggesting ground subsidence results from upward transmission. The fastest increase in fractal dimension occurs at 87.5–100 m. At 250 m, it peaks at 1.4136, indicating complex crack structures. During propulsion, the fractal dimension decreases due to upward mining space expansion through overlying rock layer collapse, forming new cracks. The proportion of mining crack area to mining space area increases gradually throughout the mining process. The present study presents a simulation model for crack identification, noting limitations in identifying tiny cracks.

Keywords: mining crack; fractal dimension; crack area; mining space

Citation: Wu, J.; Xie, D.; Yi, S.; Yin, S.; Hu, D.; Li, Y.; Wang, Y. Fractal Study of the Development Law of Mining Cracks. *Fractal Fract.* **2023**, 7, 696. https://doi.org/10.3390/fractalfract7090696

Academic Editor: Viorel-Puiu Paun

Received: 15 August 2023
Revised: 6 September 2023
Accepted: 8 September 2023
Published: 19 September 2023

1. Introduction

During coal mining activities, the stress within the rock body is redistributed, causing a disruption in the stress equilibrium of the overlying rock layer above the coal seam. This disturbance results in the subsidence and displacement of the overburden layer, ultimately leading to the formation of a complex network of staggered fractures. The evolution of mining fracture networks directly affects the permeability of coal and rock masses, as well as the transport of gases. When the evolution of mining cracks is large, geological disasters such as land subsidence and mine water inrush can occur. Therefore, studying the development of mining fractures plays a crucial role in geotechnical engineering, mining engineering, and geological disaster prevention [1–4].

In recent years, scholars have used similar simulation experiments, numerical simulations, physical simulation models, and other methods to study the deformation of overlying strata and the evolution, shape, and distribution of fractures under mining conditions. Wang et al. [5] and Liu [6] used similar simulation experiments to simulate the formation process and distribution of overburden fractures caused by mining, revealing their evolution. Studies have found that fissures develop highly discontinuous jumps. Xu et al. [7] and Huang [8] used physical simulation and field measurements to study the evolution of overlying formations and fractures caused by mining. The results show that rock separation fractures and vertical fractures occur in the overlying strata, and the overburden damage evolution is trapezoidal. Zhou et al. [9] and Wei [10] established a physical simulation model based on geological conditions, studied the distribution and evolution of mining-induced fractures in overburden strata, and extracted three typical crack networks from digital photos using image analysis. Zhou et al. [11] and Wei [12] used theoretical analysis and numerical simulation, combined with actual survey data, to study the formation and development mechanisms of ground cracks caused by coal mining. With the increase in the number of coal seams, the fracture rate and development height of the overburden increase.

Scholars have performed substantial research on cracks and microcracks using fractal theory. Numerous experiments have demonstrated that cracks in nature are fractals. The fractal property is one of the major properties of complex networks. Current research is concentrated on single-layer static networks and mesoscale applications. The fractal dimension can show the fractal properties of the network and the central nodes. Fractal properties can be used to address real problems involving network vulnerability metrics and node importance identification [13]. For example, Nayak et al. [14] proposed a generalized box count (grayscale invariant DBC) based on the fractal dimension (FD) in image analysis. The proposed model exhibits high accuracy in terms of a small fitting error when detecting surface roughness from a given dataset.

Simulations of the specimens show that fractal dimensions affect the crack growth process [15]. Liu et al. [16] studied the evolution of mining fractures and quantitatively described their fractal laws. The results demonstrate that the fractal dimension of the fractures generated by coal mining in the overlying rock undergoes two periodic changes as the coal surface advances. This fractal dimension serves as an indicator of fracture evolution and can be used for stability assessment. Wei [10] found that overburden formation pressure plays an important role in the evolution of mining-induced fractures, and the fractal dimension of fractures increases with the increase in overburden pressure. Gao et al. [17,18] used the box dimension method to quantitatively analyze the changes of coal sample cracks under different load conditions; with the increase in mining width, the fractal dimension of the crack network showed a staggered upward trend, which was divided into the rapid fracture dimension rising, slow fracture size rising, and fracture dimension stability stages. Cai [19] used the improved box counting method to measure the dynamic characterization of the extension of the fracture network in porous media, and the fractal dimensions of the fracture network were related to drying time, average pore size, moisture content, and fracture porosity, respectively. Zheng [20] combined digital image processing technology and a rock failure process analysis system to study the influence of fracture geometric distribution and microscopic heterogeneity on material structure and proposed a damage variable index based on fractal theory. Chen et al. [21,22] introduced fractal dimension to describe fracture surfaces with complex geometries and established a functional relationship between rock fracture bulk density and fractal dimension. Deng [23] proposes a three-dimensional modeling method based on discrete fracture networks and fractal theory. After mining, the lower cracks increase linearly. In higher formations, most of the cracks occur behind mining faces, and lower formations produce more cracks than the upper layers. The results of Feng [24] show that the coal crack propagation and internal crack surface show significant fractal characteristics. In addition, during dynamic loading, the multifractal feature becomes increasingly prominent. Gou [25] studied the evolution and fractal characteristics of buried rock fractures under mining disturbances. The results show that the correlation coefficient of the fractal dimension of rock fractures at different propulsion distances is greater than 0.90, and the rock fracture network under karst geomorphology has high self-similarity.

Under certain static rock stress conditions, the existence of microcomponents in coal will affect fracture abundance in similar coal reservoirs and then affect the initial permeability of the reservoir. The change in coal composition and rupture strength influence the rheological characteristics of coal system reservoirs [26]. Bandyopadhyay et al. [27] proposed the deployment of a calibrated discrete fracture network (DFN) modeling technology based on mesoscale coal images. Furthermore, a sensitivity analysis of the key fracture properties was performed to quantify their impact on coal permeability. Widely accepted predicted crack features include crack width, spacing, and number of cracks. Theodoros et al. [28] studied the mechanical factors of tensile deformation from a cracking behavior perspective, established empirical equations to predict the number of cracks, crack width and crack spacing, and predicted the average width of cracks. In addition, Jiang et al. [29] conducted hydraulic fracturing experiments using coal blocks and showed that fracture behavior at different interfaces mainly depends on the vertical stress and the interfacial friction coefficient. In the present study, a hydraulic fracture prediction model that predicts the propagation behavior of hydraulic cracks during hydraulic fracturing with high accuracy is developed.

In summary, fractal theory can be used to study the evolution and distribution characteristics of fractures, but the influence of fracture height, area, fractal dimension, and other parameters on mining activities and the propagation of fractures requires further research. In this study, the changes in shallow-buried coal seams obtained by simulating coal seam mining through similar simulation experiments were studied, and Image-Pro Plus image processing software 6.0 and Photoshop 2019 were used to identify and extract mining cracks. This paper analyzed the relationship between propulsion distance, mining crack area, coal mining space, and fractal dimension. The fracture changes of the overlying rock layer created during coal seam mining were studied based on fractal theory. The degree of rock mass failure was characterized by fractal dimensions. The development of mining fractures and their impact on the surface were predicted.

2. Materials and Methods

2.1. Experimental Method

Similarity simulation experiments are a common approach for understanding and analyzing traffic and roadway problems. It overcomes numerous inconveniences in field investigations and experiments and makes up for deficiencies in theoretical analysis.

Based on the principle of self-similarity theory, a similar material model is built on the two-dimensional similarity simulation test bench based on the ramming filling method, and the coal seam in the model is used to simulate mining. The experiment process is recorded, and the displacement, deformation, collapse, and destruction of overlying strata of coal seams after mining are captured.

2.2. Model Mining and Observation

After a similar material model is built, the mining process is simulated by tapping small wood blocks. After each tap, the overburden is waited for to halt collapsing in the mining space before advancing to the subsequent block. A coherent light source is set up for image acquisition. For instance, halogen lamps are placed around a similar analog material model, and shooting is performed after stopping the collapse after each tap of the small wood block to obtain image data. Therefore, the deformation of the overlying strata of the coal seam can be observed. Relevant image recognition software and programs are used to extract data.

3. Simulation Experiment of Mining Crack

The outline of the roadway system in the Shangwan Coal Mine is approximately rectangular, and the floor of the coal seam working face is black-gray mudstone. The overlying strata of the coal seam are mainly yellow medium-grained eolian sand, fine-grained eolian sand, loose soil, and unconsolidated soil. The simulation experiment was based on the Shangwan wellfield, and a similar engineering background material model was built based on the regional geological overview of the mine and the mechanical parameters of the rock mass. The similar material model adopts a two-dimensional similarity simulation test bench, and the ratio of the model to the actual mine is 1:250. The dimensions of the model are: length $\times$ width $\times$ height = 3200 mm $\times$ 250 mm $\times$ 870 mm. The stratification of the model is shown in Table 1. The mining model diagram is shown in Figure 1. Twenty-seven small wooden blocks were used instead of coal seam mining space, each with a width of 25 mm, corresponding to an actual distance of 12.5 m.

Table 1. Model layering scheme.

Rock Layer	Original Layer Thickness (m)	Model Layer Thickness (cm)	The Layer Number	Layer Thickness (cm)	Bulk Density	Ratio Number
Aeolian sand	6.50	2.33	1	2.60	1.79	982
Fine grained sandstone	26.95	10.48	4	10.78	1.79	655
Sandy mudstone	20.21	7.80	4	8.08	1.73	673
Medium grained sandstone	8.89	3.49	1	3.56	1.77	646
Sandy mudstone	36.70	14.21	8	14.68	1.73	673
Coarse grained sandstone	39.57	15.26	7	15.83	1.77	537
Sandy mudstone	21.90	8.15	6	8.76	1.73	673
Fine grained sandstone	33.37	12.93	10	13.35	1.79	655
Coal seam	9.26	3.49	1	3.70	0.93	682
Fine grained sandstone	23.00	8.85	3	9.20	1.79	655

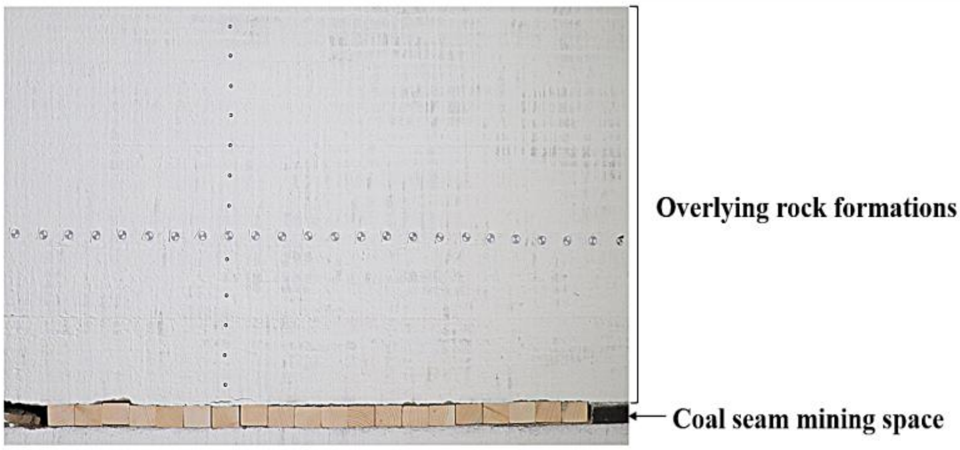

Figure 1. Mining model diagram.

After modeling similar materials, this study extracted small wooden blocks to simulate the mining process. Each small wooden block removed represents a 12.5 m propulsion distance. After each extraction, wait for the overlying rock layer to stop collapsing before continuing to extract the next wooden block until all the small wooden blocks are removed, which is equivalent to 337.5 m of mining coal seam advance. When the propulsion distance was equal to 87.5 m (the 7th small wooden block), the overlying rock layer of the coal seam began to collapse, and mining cracks appeared in the observation area. Crack image data were obtained by shooting after each twitch of the small wooden block after collapse. Thus, deformation of the overlying rock layer on the coal seam was observed. The process from the beginning of the collapse of the rock formation (the 7th block) to the last small block is shown in Figure 2.

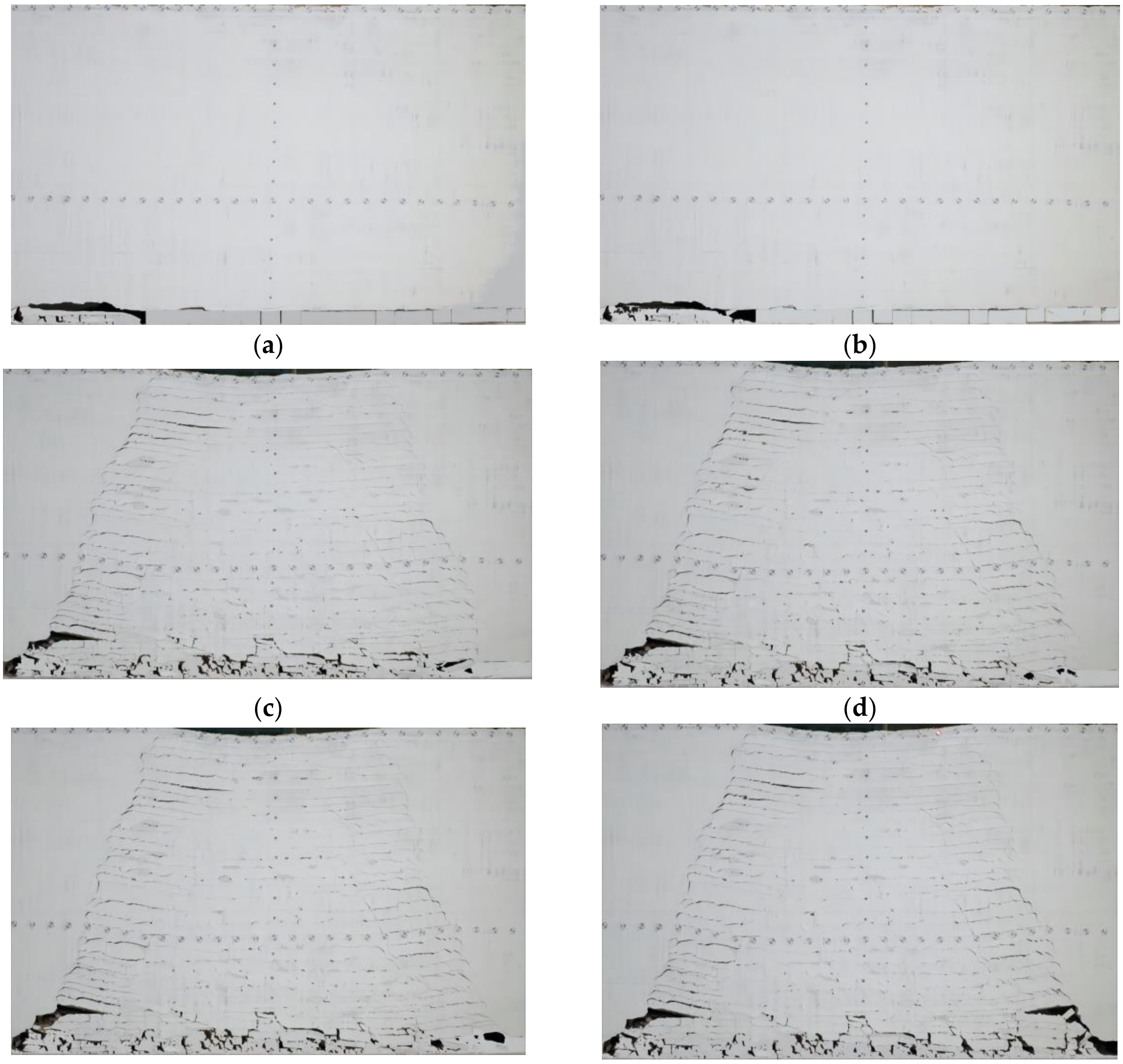

(**a**) (**b**) (**c**) (**d**) (**e**) (**f**)

Figure 2. (**a**) Propulsion 87.5 m original image (Block 7); (**b**) Propulsion 100 m original image (Block 8); (**c**) Propulsion 300 m original image (Block 24); (**d**) Propulsion 312.5 m original image (Block 25); (**e**) Propulsion 325 m original image (Block 26); (**f**)Propulsion 337.5 m original image (Block 27).

4. Image Processing and Data Analysis Simulation

4.1. Fractal Theory

In fractal geometry, the box dimension is a method of measuring the fractal dimension in distance spaces, such as Euclidean space R. In practical applications, the box dimension can be understood as constructing squares (bodies, called boxes) with sides of r to cover the set (which can be a line, surface, or volume), calculating the number of "boxes" with different r values and F intersecting N(r), and box dimension D can be obtained from the slope value of the straight line in the double logarithmic coordinate system of N(r) and r. D is the box dimension of traditional scale r and characterizes the efficiency of a small set of the same shape covering a universal set. Box dimensions can be defined as:

$$\dim_{\text{box}}(s) = \lim_{r \to 0} \frac{\log N(r)}{\log(1/r)} \tag{1}$$

Box counting is commonly used to determine D, originally defined by [30].

$$N(r) \sim r^{D_f} \tag{2}$$

Equation (2) is called the fractal scale law, where N(r) represents the number of boxes occupied by pixels, and r is the size of the box or scale used to measure stellar islands/clouds/galaxies.

4.2. Fractal Dimension

We used Photoshop software to color correct images, denoise, reduce background interference, and reduce calculation errors. Image-Pro Plus was used to binarize the cropped pictures, and then the fractal dimension of the mining crack was calculated based on the box dimension method using MATLAB 2021a. The image binarization effect and the MATLAB calculation result for an advancement of 175 m (Block 14) are shown in Figure 3. The full calculation results are shown in Table 2.

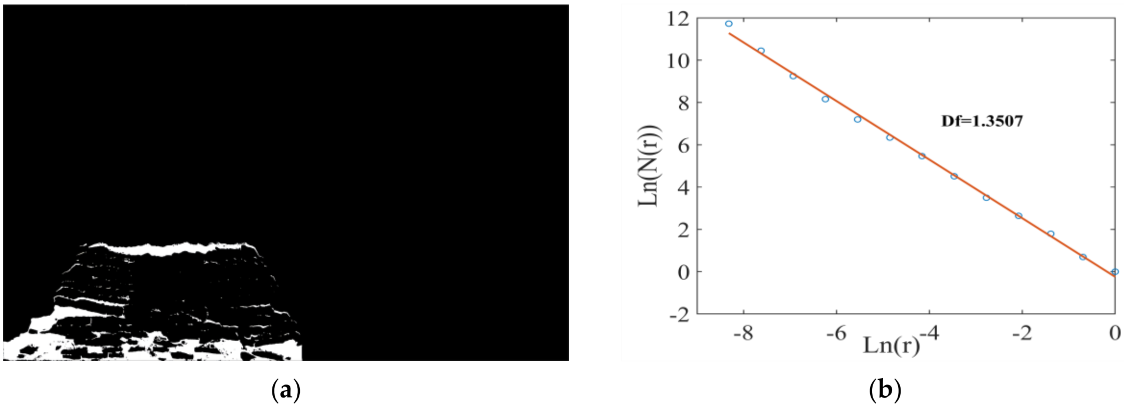

Figure 3. (**a**) Advance (Block 14) 175 m binarized image; (**b**) fractal dimension calculation at 175 m in advance (Block 14).

Table 2. Table of fractal dimension calculation results.

The Number of Small Wooden Blocks That Are Propelled	Propulsion Distance (m)	Fractal Dimension	Error of the Fractal Dimensions
7	87.5	1.2559	0.0000
8	100.0	1.2950	−0.0015
9	112.5	1.3345	0.0049
13	162.5	1.3644	0.0023
14	175.0	1.3507	−0.0051
17	212.5	1.3717	0.0001
18	225.0	1.3885	−0.0069
20	250.0	1.4136	0.0242
21	262.5	1.3780	−0.0461
22	275.0	1.4070	0.0454
23	287.5	1.3737	−0.0250
24	300.0	1.3697	0.0026
25	312.5	1.3730	0.0018
26	325.0	1.3746	−0.0067
27	337.5	1.3905	0.0000

From Table 3 and the percentage increase in fractal dimension with propulsion distance, the fractal dimension is shown to increase with the increase in propulsion distance. This suggests that the complexity of mining-induced fractures grows as the propulsion distance increases. At a propulsion distance of 87.5 m, the overlying rock layer of the coal seam began to collapse, and mining cracks appeared in the observation area. The mining crack structure was the simplest at this time. At a propulsion distance of 250 m, the fractal dimension reached its maximum, indicating that the mining crack structure was the most complex at this time.

Table 3. Percentage growth of fractal dimension.

Propulsion Process (m)	Fractal Dimension Changes	Percentage Growth in Fractal Dimension
87.5–100.0	1.2559–1.2950	3.11%
100.0–112.5	1.2950–1.3345	3.05%
112.5–162.5	1.3345–1.3644	2.24%
162.5–175.0	1.3644–1.3507	−1.00%
175.0–212.5	1.3507–1.3717	1.55%
212.5–225.0	1.3717–1.3885	1.22%
225.0–250.0	1.3885–1.4136	1.81%
250.0–262.5	1.4136–1.3780	−2.52%
262.5–275.0	1.3780–1.4070	2.10%
275.0–287.5	1.4070–1.3737	−2.37%
287.5–300.0	1.3737–1.3697	−0.29%
300.0–312.5	1.3697–1.3730	0.24%
312.5–325.0	1.3730–1.3746	0.12%
325.0–337.5	1.3746–1.3905	1.16%

When advancing from 87.5 to 100 m, the fractal dimension increased from 1.2559 to 1.2950, a total of 3.11%; the percentage increase in this stage was the largest in the selected observation images, indicating that the damage and failure transmission of mining cracks was the fastest. When advancing from 312.5 to 325 m, the fractal dimension increased from 1.3730 to 1.3746, a total of only 0.12%; the percentage increase in fractal dimension at this stage was the smallest in the selected observation images (Figure 4), indicating that the damage and failure conduction of mining cracks was the slowest.

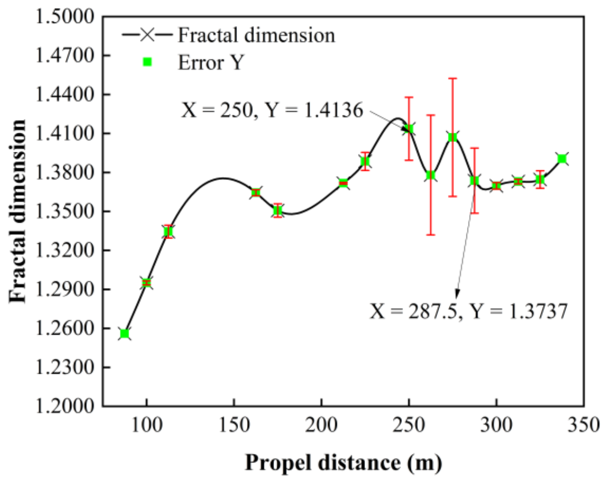

Figure 4. Fractal dimension and a propulsion distance plot.

Although the fractal dimension exhibits an overall upward trend with the increase in the advancing distance, the change in fractal dimension is significant during the advance from 250 to 287.5 m, and the line chart of fractal dimension changes with the advancing distance is shown as an approximate wavy line.

4.3. Mining Crack Area

The image parameters were extracted using Image-Pro Plus, and mining space area data, mining fracture area data, mining crack area data of overlying coal seams, and mining fracture area data in mining space are listed in Table 4. Details of these areas are shown in Figure 5.

Table 4. Mining area and mining crack area.

Propulsion Distance (m)	Fractal Dimension	Mining Crack Area Data (cm^2)	Mining Crack Area of Overlying Coal Seam S1 (cm^2)	Mining Fracture Area in Mining Space S2 (cm^2)	Mining Area S (cm^2)
87.5	1.2559	69.19873	31.88597	37.31276	127.33084
100.0	1.2950	78.04105	30.94653	47.09452	146.20998
112.5	1.3345	95.41902	61.84787	33.57115	162.68079
162.5	1.3644	163.81067	109.55578	54.25489	236.17639
175.0	1.3507	185.72440	129.79079	55.93361	254.90379
225.0	1.3885	216.32550	168.72414	47.60136	324.06072
250.0	1.4136	260.07226	190.37961	69.69265	357.71567
262.5	1.3780	285.79540	188.42003	97.37537	376.46887
275.0	1.4070	339.95989	225.80058	114.15931	393.85330
287.5	1.3737	296.40685	201.84333	94.56352	412.35750
300.0	1.3697	291.98729	199.51895	92.46834	437.66464
312.5	1.3730	279.47761	204.03534	75.44226	454.78760
325.0	1.3746	308.02875	213.30059	94.72816	470.89362
337.5	1.3905	349.14444	243.84036	105.30408	483.76484

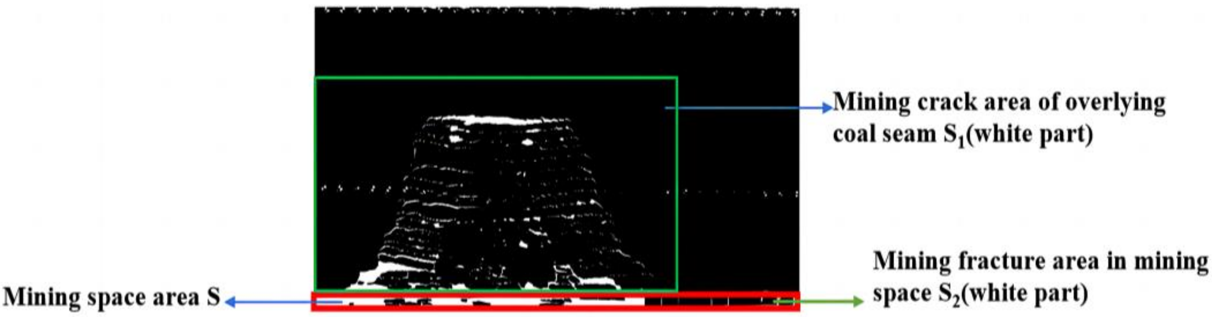

Figure 5. Area schematic diagram.

In the propulsion phase from 250 to 287.5 m, the fractal dimension changes with the propulsion distance, and the line chart appears as an approximate wavy line. The advancement process at this stage was analyzed; from the data of the mining crack area (Table 4), the mining crack areas at 250, 262.5, 275, and 287.5 m were found to be 260.07662, 285.79540, 339.95989, and 296.40685 cm^2, respectively. The relationship between the fractal dimension and the mining crack area cannot be seen from the area change.

Using a section selection tool, the binarized images at 250, 262.5, and 275 m were divided into ten aliquots of landscape orientation. The slice results are shown in Figure 6. The area data identified and extracted are shown in Table 5. According to Table 5, When advancing from 250 to 275 m, new large-scale mining cracks appeared in slices 1–3, collapsed in slices 4, did not change significantly in slices 5–9, and increased greatly in area in slice 10 owing to the increase in propulsion distance. Combined with the fractal dimension, the area change in slices 1–4 was studied. The following conclusions were drawn: when the fractal dimension of the mining crack area increases, a large area of the formed mining crack collapses and compacts, and a large area expansion occurs vertically and horizontally to form a new mining crack, which is the main factor for the decrease in the fractal dimension of the area increase. After the mining crack is compacted, as advancement continues, the mining crack area increases. The compacted part does not change significantly, and a new collapse and mining crack form in the mining space; the fractal dimension also increases.

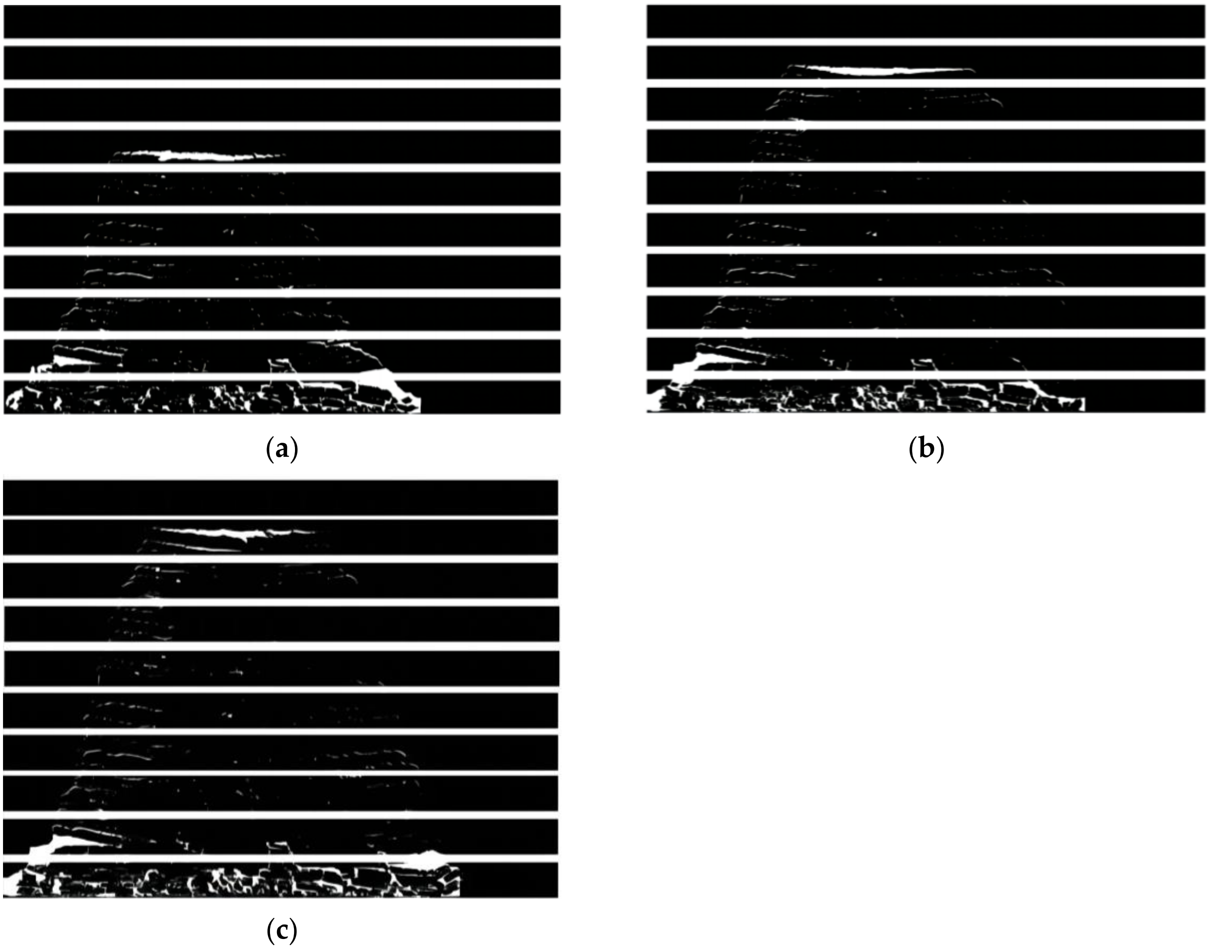

Figure 6. (a) Horizontal section when advancing 250 m (Block 20); (b) Horizontal section when advancing 262.5 m (Block 21); (c). Horizontal section when advancing 275 m (Block 22).

Table 5. Section mining fracture area comparison.

Serial Number	Propulsion 250 m		Propulsion 262.5 m		Propulsion 275 m	
	Pixel	Area	Pixel	Area	Pixel	Area
1	0	0	0	0	6	0.01844
2	0	0	15,280	46.97252	14,151	43.50184
3	0	0	2550	7.83900	3081	9.47136
4	14,014	43.08069	1254	3.85494	1379	4.23921
5	1254	3.85494	1181	3.63053	1618	4.97392
6	1644	5.05385	1730	5.31822	2006	6.16668
7	2916	8.96413	2688	8.26323	3302	10.15074
8	3170	9.74495	2378	7.31025	3622	11.13446
9	16,973	52.17701	15,962	49.06907	18,032	55.43250
10	42,715	131.31095	49,115	150.98531	62,966	193.56492
aggregate	82,686	254.18652	92,138	283.24309	110,163	338.65407

4.4. Connection between Mining Cracks and Mining Spaces

Table 6 compares mining fracture area S1 of the overlying rock layer of the coal seam for each propulsion distance and mining fracture area S2 in the mining space with the total area. A line chart of the percentage of mining fracture area in the overlying rock layer as a function of the mining space area is plotted in Figure 7.

Table 6. The proportion of mining fracture area S1 and mining fracture area S2 in the overlying rock layer of the coal seam.

Propel Distance (m)	S1/Mining Area S	S2/Mining Area S
87.5	25.04%	29.30%
100.0	21.17%	32.21%
112.5	38.02%	20.64%
162.5	46.39%	22.97%
175.0	50.92%	21.94%
212.5	49.54%	20.29%
225.0	52.07%	14.69%
250.0	53.22%	19.48%
262.5	50.05%	25.87%
275.0	57.33%	28.99%
287.5	48.95%	22.93%
300.0	45.59%	21.13%
312.5	44.86%	16.59%
325.0	45.30%	20.12%
337.5	50.40%	21.77%

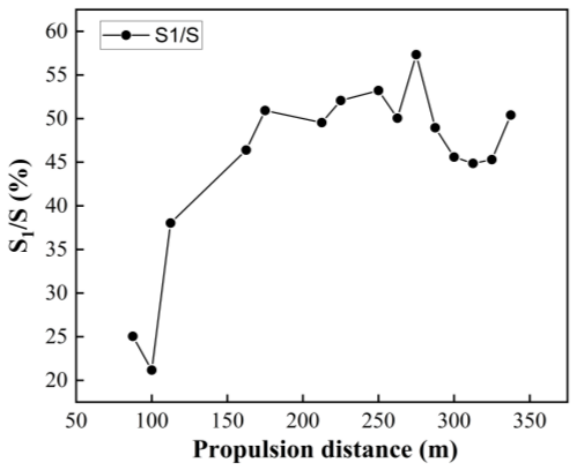

Figure 7. Percentage of mining fractures in mining space area in overlying rock layer line.

When advancing 87.5 m, the mining crack area of the overlying rock mass of the coal seam accounted for 25.04% of the mining space, and the intermediate process increased as a whole, although there were slight undulations. When it advanced to 337.5 m, it finally conducted to the surface to form a subsidence basin, at which time the mining cracks of the overlying rock mass accounted for 50.4% of the mining space. With the increase in the propulsion distance, the percentage of mining fracture area for the overlying rock mass increases in the mining space; that is, the overall upward propagation of the mining space is enhanced as the cracks widen.

Figure 7 shows that the change rate of the mining crack area of the overlying rock mass for each propulsion distance to the mining space area has two slower parts, which are from 175 to 262.5 m and 287.5 to 337.5 m. In these two areas, the change in the percentage of the mining fracture area of the overlying rock layer was relatively slow, but both first decreased and then increased. This is because the mining space propagates upwards in a separatory manner, and the overlying rock layer on the coal seam collapses, filling in the old mining cracks to form new ones and gradually compacting in the process.

From Table 6, the ratio of mining fracture area to mining space area is shown to be relatively stable, and the average value is 22.59%. Pores left by the collapse of the overlying rock layer create the new “cracks”. However, these are not true mining cracks; therefore, the transmission of the mining cracks in the mining space is uniform.

In the mining process, the cracks were distributed in a trapezoidal shape, and a certain height formed during the upward propagation. The fracture height of the image at different propulsion distances was measured, and then the statistics were calculated. The results are shown in Table 7.

Table 7. Statistical table of fracture development height.

Propel Distance (m)	Mean Value of Fracture Development Height (m)	Minimum Fracture Development Height (m)	Fissure Development Height Maximum (m)
87.5	11.52218	8.94957	12.8692
100.0	11.57414	8.94335	12.8609
112.5	21.40552	19.1526	22.5522
162.5	30.22002	27.4827	33.1722
175.0	60.00075	58.009	62.47
212.5	59.55289	57.7243	61.8436
225.0	120.4479	118.586	121.996
250.0	120.001	119.033	121.627
262.5	160.48	158.378	162.33
275.0	167.6193	166.038	169.451
287.5	190.8538	188.655	193.279
300.0	190.3442	187.77	193.721
312.5	190.5738	187.824	193.892
325.0	189.9195	187.499	193.587
337.5	190.2236	187.56	193.623

The average value of fracture height was selected to study the mining process. In Figure 8, the correlation coefficient between the fractal dimension and the advancing distance is 0.56, indicating that the correlation between the fractal dimension and the advancing distance is not high, which is due to the subsequent compaction process during the advancing process.

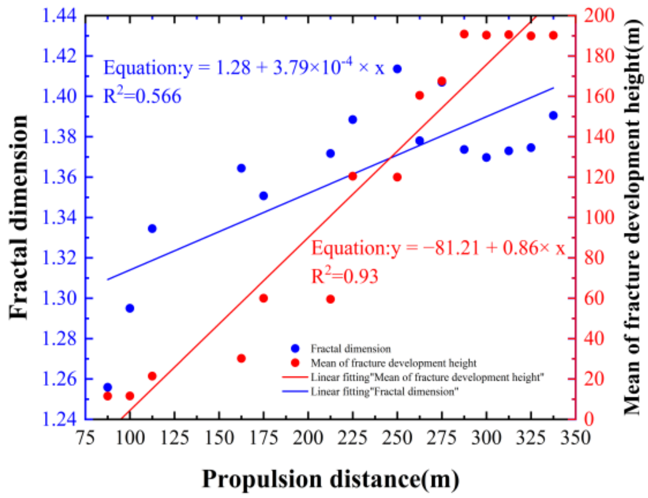

Figure 8. Fractal dimension, fracture development height average, and propulsion distance.

Figures 8 and 9 show that the propulsion distance is positively correlated with the fracture development height and mining fracture area of the overlying rock layer. The correlation coefficient reaches 94%. The height of fissure development varies significantly with propulsion distance.

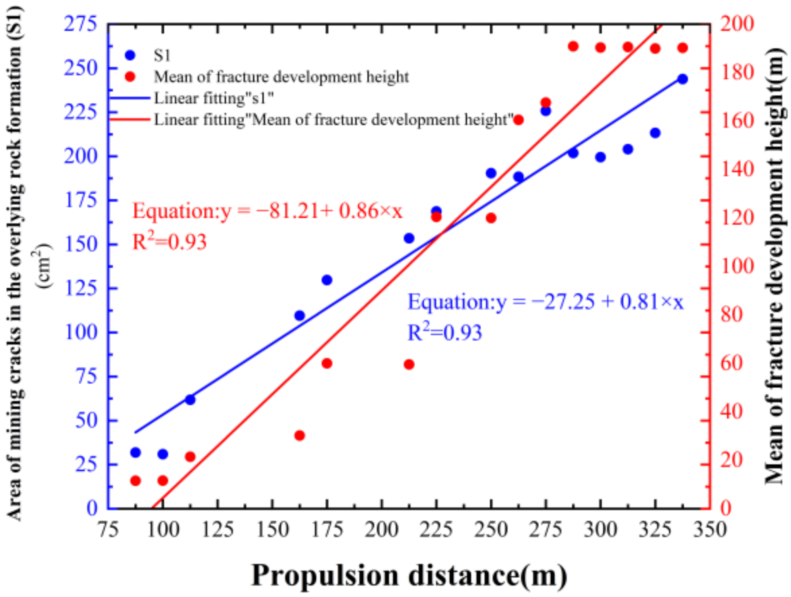

Figure 9. Relationship between mining fracture area, fracture development height, and propulsion distance in the overlying rock layer.

4.5. Conduction Law of Mining Cracks

To study the conduction law of mining fractures, we must study the spatial distribution of mining cracks in rock formations during the final transmission to the surface, forming a surface subsidence basin. During the final propagation of the mining crack to the surface, the surface subsidence basin advanced to 337.5 m. This is depicted in Figures 10 and 11, which is divided into ten parts evenly in the horizontal and vertical directions after the cropping operation.

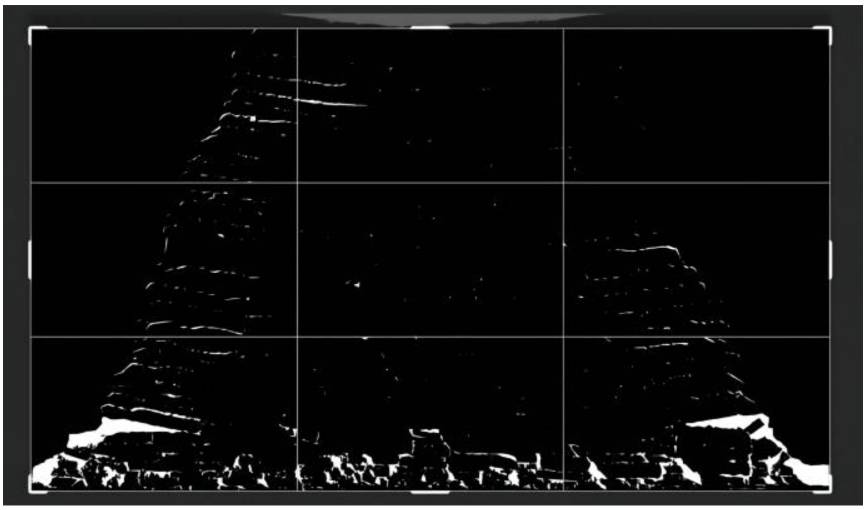

Figure 10. Cutting of mining fracture area.

Number of slices: Horizontal slices are numbered from top to bottom; vertical slices are numbered from left to right, 1–10. We used Photoshop to count the number of pixels and calculate the area of the measured area based on the conversion relationship between pixels and area. The data are listed in Table 8. The percentage of mining cracks in the horizontal and vertical slices is plotted, and the results are shown in Figure 12.

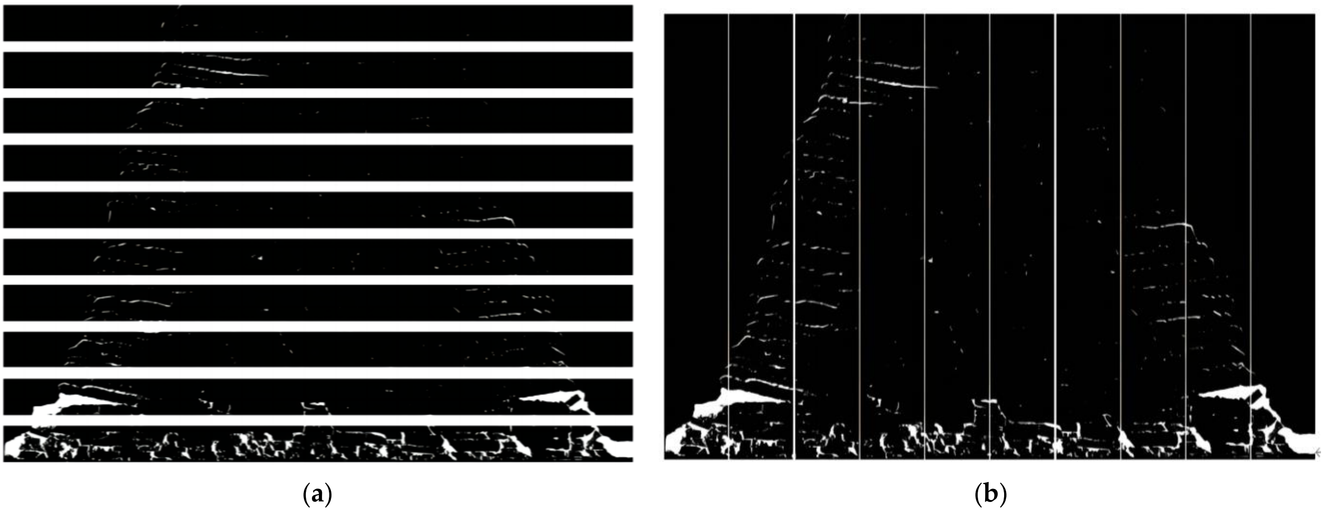

Figure 11. (**a**) Horizontal slice; (**b**) Vertical slice.

Table 8. Horizontal slice and vertical slice mining fracture area and proportion of mining space area. Area and proportion of mining space area.

Serial Number	The Area of Cracks Mined in Each Horizontal Section S1	The Area of Cracks in Each Vertical Section S2	Mining Space Area S	S1/S	S2/S
1	1.02676	46.07181	461.22223	0.22%	9.99%
2	10.00625	38.43262		2.17%	8.33%
3	3.27086	23.51085		0.71%	5.10%
4	2.28100	19.79732		0.49%	4.29%
5	4.99237	16.81850		1.08%	3.65%
6	6.21894	12.21347		1.35%	2.65%
7	9.04713	13.77512		1.96%	2.99%
8	8.17715	20.47977		1.77%	4.44%
9	73.46220	35.15869		15.93%	7.62%
10	152.86974	45.09424		33.14%	9.78%
aggregate	271.35240	271.35240		58.83%	58.83%

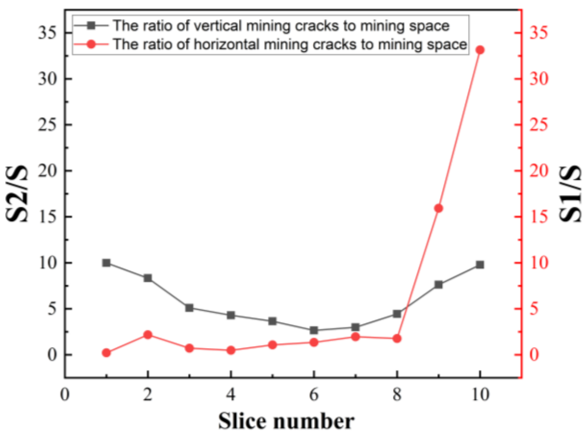

Figure 12. Broken-line diagram of horizontal slice and vertical slice mining fractures.

The horizontal slices reflect the propagation of the mining crack in the vertical direction, and the vertical slice reflects that in the horizontal direction.

Mining cracks propagate from the bottom up; thus, when studying the propagation law of mining cracks, it is logical to look at the transverse sections starting with slice 10. Slices 9 and 10 were divided into the first part, and the percentage of the mining crack area to mining space area exhibited a sharp and significant decrease, indicating that mining cracks were denser in these two slices. Slices 1–8 were divided into the second part, and the percentage value of the mining crack area to the mining space area was evenly distributed; the average value was 1.22%. Figure 12 shows that the mining crack gradually weakens when propagating vertically because it has been repeatedly compacted and closed, forming new mining cracks until ground subsidence occurs. The new mining cracks are formed in the upper layer of the compacted rock layer.

Similarly, in the vertical slices, the slice is divided into two parts. Slices 1–2 and 9–10 are the first part, and slices 3–8 are the second part. The average value of the first part is 8.93%, and that of the second part is 3.85%. Within these two parts, the distribution of mining cracks is relatively uniform. In the second part, the percentage of mining crack area to mining space area is considerably smaller than that of the first part, because the second part is located in the middle of the mining space, and its comprehensive rock and soil stress is less than that at both ends. Thus, it is more prone to collapse, compaction, and closure.

Based on the data in Table 8, the total percentage of mining cracks in the rock formation in the mining space is:

$$\frac{S_1}{S} = \frac{271.35}{461.22} \times 100\% = 58.83\%$$

which is significantly smaller than the mining space area and is primarily caused by the propagation of the mining space from bottom to top through separation. Theoretically, the subsidence area of the earth can be calculated.

$$A_{s1} = \left(1 - \frac{S_1}{S}\right) \times S = 189.8\ \mathrm{cm}^2 \tag{3}$$

The actual surface subsidence area was calculated by Photoshop and was $A_{s2} = 75.33\ \mathrm{cm}^2$.

In Equation (3), A is the subsidence area, S_1 is the mining fracture area, and S is the mining space area.

The swelling of rock is mainly characterized by soft rock, and the volume of roof rock in the goaf area increases. The broken expansion coefficient is usually described by the fracture height.

$$k = \frac{H_1}{H_1 - H_2} = \frac{193.623}{193.623 - 8.73} = 1.05 \tag{4}$$

In Equation (4), k is the broken expansion coefficient, H_1 is the fissure development height maximum, and H_2 is the thickness of the coal seam.

These data show that the broken expansion coefficient reached 1.05 during mining, indicating that the fragmentation expansion was created and the area increased.

5. Conclusions

1. The fractal dimension increases the fastest when advancing from 87.5 to 100 m; therefore, the mining crack conducts the fastest at this stage. When advancing to 250 m, the fractal dimension reached a maximum value of 1.4136, indicating that the mining crack structure was the most complex. During propulsion, the fractal dimension has a negative growth because the mining space propagates upward in a separational manner and the overlying rock layer on the coal seam collapses, filling in the old mining cracks to form new mining cracks and gradually compacting.
2. During the entire mining process, the percentage of the mining crack area of the overlying rock layer in relation to the mining space area gradually increases; that is, the mining crack gradually increases when the mining crack propagates upward. The

mining crack is formed by the collapse of the overlying rock layer in the mining space. Thus, the ratio of the mining crack area to the mining space area is relatively stable. However, the mining crack area in the middle of the mining space is slightly smaller than the two ends.

3. The propulsion distance is positively correlated with the fracture development height and mining fracture area of the overlying rock layer. The correlation coefficient reaches 94%. The height of fissure development varies significantly with propulsion distance.
4. The percentage of mining fracture area in the mining space area during the final transmission of the mining crack to the surface was analyzed to study the propagation of the mining fracture and its final impact on the surface. The distribution of mining cracks is relatively uniform in the horizontal direction, and the distribution in the vertical direction is gradually weakened; therefore, the propagation of mining cracks is gradually reduced. Slices 9 and 10 are concentrated areas of mining cracks, and the structure of mining cracks is also more complex. The area of mining cracks is significantly smaller than the area of mining space.
5. In conclusion, future research in this field should aim to address the limitations of current methods, enhance our understanding of mining crack behavior, and develop practical solutions to minimize the risks associated with mining cracks in both underground and surface mining operations.

Author Contributions: Methodology, S.Y. (Sihai Yi) and J.W.; formal analysis, Y.L.; investigation, Y.W.; resources, D.H.; data curation, S.Y. (Shangxian Yin); writing—original draft, D.X.; writing—review and editing, J.W. and D.X.; funding acquisition S.Y. (Sihai Yi) and S.Y. (Shangxian Yin). All authors have read and agreed to the published version of the manuscript.

Funding: This research was funded by National Natural Science Foundation of China (52274165), National Natural Science Foundation of China (51974126), National Natural Science Foundation of China (51204069) and Funding Projects for Basic Scientific Research Business Fees in Central Universities (3142015093).

Data Availability Statement: Not applicable.

Conflicts of Interest: The authors declare no conflict of interest.

References

1. Wang, Z.G.; Zhou, H.W.; Xie, H.P. Research on fractal characterization of mined crack network evolution in overburden rock stratum under deep mining. *Rock Soil Mech.* **2009**, *30*, 2403–2408.
2. Cheng, Y.P.; Yu, Q.X.; Yuang, L. Experimental research of safe and high-efficient exploitation of coal and pressure relief gas in long distance. *J. China Univ. Min. Technol.* **2004**, *33*, 132–136.
3. Liu, Z.G.; Liang, Y. Study on coal seam roof gas drainage from the strike of annular fracture areas by the long drill method. *Eng. Sci.* **2004**, *6*, 32–38.
4. Tu, M. Study on the growth height of separation fracture of mining rock in Panxie area. *Mei T'an Hsueh Pao* **2004**, *29*, 641–645.
5. Wang, C.; Zhang, N.C.; Han, Y.F.; Xiong, Z.Q.; Qian, D.Y. Experiment research on overburden mining-induced fracture evolution and its fractal characteristics in ascending mining. *Arab. J. Geosci.* **2015**, *8*, 13–21. [CrossRef]
6. Liu, X.Y. Experimental Study of Dynamic Development and Fractal law of Mining Rock Fracture. *Appl. Mech. Mater.* **2011**, *71*, 3428–3432. [CrossRef]
7. Xu, X.L.; Zhang, N.; Tian, S.C. Mining-induced movement properties and fissure time-space evolution law in overlying strata. *Int. J. Min. Sci. Technol.* **2012**, *22*, 817–820. [CrossRef]
8. Huang, Q.X.; He, Y.P.; Cao, J. Experimental investigation on crack development characteristics in shallow coal seam mining in China. *Energies* **2019**, *12*, 1302–1318. [CrossRef]
9. Zhou, H.W.; Liu, J.F.; Xue, D.J.; Yi, H.Y.; Xue, J.H. Numerical simulation of gas flow process in mining-induced crack network. *Int. J. Min. Sci. Technol.* **2012**, *22*, 793–799. [CrossRef]
10. Wei, X.J.; Gao, M.Z.; Lv, Y.C.; Shi, X.C.; Gao, H.L.; Zhou, H.W. Evolution of a mining induced fracture network in the overburden strata of an inclined coal seam. *Int. J. Min. Sci. Technol.* **2012**, *22*, 779–783. [CrossRef]
11. Zhou, D.W.; Wu, K.; Bai, Z.H.; Hu, Z.Q.; Li, L.; Xu, Y.K.; Diao, X.P. Formation and development mechanism of ground crack caused by coal mining: Effects of overlying key strata. *Bull. Eng. Geol. Environ.* **2019**, *78*, 1025–1044.

12. Yang, W.F.; Ji, Y.B.; Shen, D.Y.; Xia, X.H. Discrete element numerical simulation of crack evolution in multi-coal seam mining. In Proceedings of the International Conference on Computer Application and System Modeling, Taiyuan, China, 22–24 October 2010; pp. 383–385.
13. Wen, T.; Cheong, K.H. The fractal dimension of complex networks: A review. *Inf. Fusion* **2021**, *73*, 87–102. [CrossRef]
14. Nayak, S.R.; Mishra, J. Fractal dimension-based generalized box-counting technique with application to grayscale images. *Fractals* **2021**, *29*, 17. [CrossRef]
15. Chang, X.; Ren, M.F.; Guo, X. A cohesive zone model for self-similar fractal crack propagation. *J. Mech. Sci. Technol.* **2017**, *31*, 4763–4769.
16. Liu, C.; Xue, J.H.; Yu, G.F.; Cheng, X.Y. Fractal characterization for the mining crack evolution process of overlying strata based on microseismic monitoring technology. *Int. J. Min. Sci. Technol.* **2016**, *26*, 295–299. [CrossRef]
17. Gao, M.Z.; Xie, J.; Guo, J.; Lu, Y.Q.; He, Z.Q.; Li, C. Fractal evolution and connectivity characteristics of mining-induced crack networks in coal masses at different depths. *Géoméch. Geophys. Geo-Energy Geo-Resour.* **2021**, *7*, 1–15. [CrossRef]
18. Gao, M.Z.; Zhang, J.G.; Li, S.W.; Wang, M.; Wang, Y.W.; Cui, P.F. Calculating changes in fractal dimension of surface cracks to quantify how the dynamic loading rate affects rock failure in deep mining. *J. Cent. South Univ.* **2020**, *27*, 3013–3024. [CrossRef]
19. Cai, J.C.; Wei, W.; Hu, X.G.; Liu, R.C.; Wang, J.J. Fractal characterization of dynamic fracture network extension in porous media. *Fractals* **2017**, *25*, 1750023. [CrossRef]
20. Zheng, L.L.; Liu, H.; Zuo, Y.J.; Zhang, Q.P.; Lin, W.; Qiu, Q.; Liu, X.R.; Liu, Z.Q. Fractal study on the failure evolution of concrete material with single flaw based on DIP technique. *Adv. Mater. Sci. Eng.* **2022**, *2022*, 1–15. [CrossRef]
21. Chen, Y.; Jin, Y.; Chen, M.; Yi, Z.C.; Zheng, X.J. Quantitative evaluation of rock brittleness based on the energy dissipation principle, an application to type II mode crack. *J. Nat. Gas Sci. Eng.* **2017**, *45*, 527–536. [CrossRef]
22. Ma, D.; Duan, H.G.; Liu, J.F.; Li, X.B.; Zhou, Z.L. The role of gangue on the mitigation of mining-induced hazards and environmental pollution: An experimental investigation. *Sci. Total Environ.* **2019**, *664*, 436–448. [CrossRef] [PubMed]
23. Deng, G.D.; Xie, H.P.; Gao, M.Z.; Li, C.; He, Z.Q. Numerical simulation on the evolution of mining-induced fracture network in a coal seam and its overburden under the top coal caving method. *Adv. Civ. Eng.* **2020**, *2020*, 6077187. [CrossRef]
24. Feng, J.J.; Wang, E.Y.; Huang, Q.S.; Ding, H.C.; Dang, L. Time-varying multifractal analysis of crack propagation and internal fracture process of coal under dynamic loading. *Fractals* **2021**, *29*, 2150089. [CrossRef]
25. Gou, R.T.; Jiang, C.Y.; Liu, Y.; Wang, C.; Li, Y.L. Study on fractal characteristics of evolution of mining-induced fissures in Karst landform. *Energies* **2022**, *15*, 5372. [CrossRef]
26. Mukherjee, S.; Rajabi, M.; Esterle, J. Relationship between coal composition, fracture abundance and initial reservoir permeability: A case study in the Walloon Coal Measures, Surat Basin, Australia. *Int. J. Coal Geol.* **2021**, *240*, 103726. [CrossRef]
27. Bandyopadhyay, K.; Mallik, J. An optimum solution for coal permeability estimation from mesoscopic scale calibrated stochastic and deterministic discrete fracture network models. *Fuel* **2023**, *331*, 125626. [CrossRef]
28. Theodoros, A.C.; Vassilis, P.P. Experimental investigation on cracking behavior of reinforced concrete tension ties. *Case Stud. Constr. Mater.* **2022**, *16*, e00810.
29. Jiang, Y.; Lian, H.; Nguyen, V.P.; Liang, W. Propagation Behavior of Hydraulic Fracture across the Coal-rock Interface under Different Interfacial Friction Coefficients and A New Prediction Model. *J. Nat. Gas Sci. Eng.* **2019**, *68*, 102894. [CrossRef]
30. Yu, B.M. Analysis of flow in fractal porous media. *Appl. Mech. Rev.* **2008**, *61*, 050801. [CrossRef]